ISBN: 978-628-96613-3-0. ISSN: 2414-6390. Digital Object Identifier: https://dx.doi.org/10.18687/LACCEI2026.1.1.756

Implementation of an Environmental Monitoring System Using Autonomous Unmanned Vehicles

Jorge Cardé Santiago[1], Nathalia Cotto Figueroa[1], Jordi A. Farre Sabillon[1],
Josejomar Rivera Flecha[1], Daniel Miranda Navarro[1], Gabriel Valentin Galarza[1], Diego Aponte-Roa[1]
[1]Universidad Ana G. Méndez, Puerto Rico, Electrical and Computer Engineering Department
jcarde5@email.uagm.edu, ncotto52@email.uagm.edu, jfarre3@email.uagm.edu, jrivera2867@email.uagm.edu,
dmiranda54@email.uagm.edu, gvalentin49@email.uagm.edu, aponted1@uagm.edu

***Abstract*—This paper presents the design and implementation of an autonomous environmental monitoring platform based on an unmanned aerial vehicle equipped with a Pixhawk 6C flight controller and a dual ESP32 master-slave sensing architecture. The onboard ESP32 functions as the sensing node and interfaces with the selected gas and environmental sensors, while the receiving ESP32 or monitoring station records the transmitted data through a Wi-Fi link. Sensor data may also be transmitted to the Pixhawk through custom MAVLink messages, providing a redundant communication channel when Wi-Fi coverage degrades. The integrated system supports waypoint missions, modular power distribution, and real-time telemetry for repeatable data collection flights. Tests were conducted in Caguas, Juncos, and Gurabo, Puerto Rico, using the same ESP32-based sensing architecture, with the sensor set modified according to each test campaign. Results demonstrate a scalable low-cost method for geo-referenced environmental monitoring using open-source hardware suitable for multi-vehicle deployments.**

***Keywords*—Autonomous UAV, Environmental monitoring, ESP32 microcontroller, Gas sensor networks, MAVLink telemetry.**

I. Introduction

Unmanned aerial vehicles (UAVs) have emerged as effective platforms for environmental monitoring in areas that are difficult to access using traditional ground-based systems. Their ability to carry embedded sensing hardware, rapidly deploy across constrained environments, and follow predefined autonomous trajectories enables high-resolution, geo-referenced data acquisition with broad spatial coverage [1]. These capabilities have supported UAV applications in air-quality monitoring, agriculture, climate-sensitive ecosystem observation, disaster response, and search-and-rescue missions [2]–[4].

Embedded platforms such as ESP32 microcontrollers provide low-power computation, wireless communication, and flexible sensor interfacing for distributed environmental monitoring [5]. When integrated with open-source flight controllers and MAVLink telemetry, these platforms support modular UAV architectures and reliable data transmission under limited-bandwidth conditions [6]. MAVLink is a lightweight telemetry protocol explicitly designed for operation over unreliable low-bandwidth radio links, and is widely adopted for communication between vehicles and ground control stations [7]–[10]. Although standardized MAVLink message sets are preferred over project-specific dialects to reduce long-term maintenance [11], customized messaging could be used to support the sensing payload.

This paper presents an autonomous UAV-based environmental sensing platform that integrates a Pixhawk 6C flight controller with an ESP32-based data acquisition system. A dual ESP32 master-slave architecture is used for wireless sensing and data logging. The onboard ESP32 operates as the sensing node, while the receiving ESP32 or monitoring station records transmitted measurements for analysis.

The sensor set was modified between test campaigns without changing the general sensing architecture. Caguas and Juncos measurements used MQ-series gas sensors for pollutant-equivalent trend analysis, while Gurabo measurements used MQ-2 and MQ-9 gas sensors with a BME/BMP280 environmental sensor for temperature, humidity, and pressure context for interpreting MQ sensor behavior, since metal-oxide semiconductor sensors are affected by temperature, humidity, and airflow. Sensor data is transmitted wirelessly for logging and analysis, while selected measurements can also be transmitted through MAVLink telemetry for redundancy during flight operations.

The organization of this paper is as follows: Section II details the design of the proposed system. Section III describes the testing conditions. Section IV discusses the experimental results. Finally, Section V provides a summary of the findings and conclusions.

II. Proposed System

A. System Description

The proposed system consists of an autonomous UAV platform designed to collect geo-referenced environmental data during flight. The system was developed to include autonomous flight capabilities, autonomous image recognition based on ArUco fiducial markers [12], [13], and geo-referenced telemetry-controlled missions using the Mission Planner platform. The UAV integrates a Pixhawk 6C flight controller, which manages stabilization, navigation, and execution of predefined waypoint missions.

The sensing system uses a dual ESP32 master-slave architecture for wireless acquisition. The onboard ESP32 functions as the sensing node, interfacing with the selected MQ-series gas sensors and environmental sensors according to the test configuration. The receiving ESP32 or monitoring station

Figure 1. Drone Isometric View

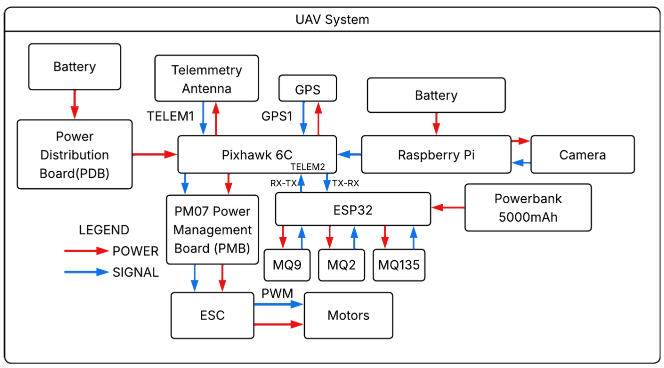

Figure 2. UAV Hardware Block Diagram

records transmitted measurements for storage and analysis. For the Gurabo tests, MQ-2 [14], MQ-9 [15], and BME/BMP280 measurements were used to evaluate combustible-gas trends and environmental context. Sensor data is transmitted through Wi-Fi from the sensing node to the receiving system, where readings are logged in CSV format. In parallel, selected processed measurements can be forwarded to the Pixhawk and transmitted through MAVLink telemetry as a redundant communication path.

The UAV frame includes a power distribution board (PDB), GPS receiver, telemetry radio, and electronic speed controllers (ESCs), allowing the platform to operate as a modular solution for autonomous environmental monitoring missions (see Fig. 1). The Pixhawk 6C flight controller includes STM32H7-class processing architecture and redundant inertial sensing modules that enable reliable autonomous waypoint execution while handling telemetry and payload integration [16]–[18].

B. Design Details

Fig. 2 shows the UAV hardware architecture, including the battery, PDB, Pixhawk, ESCs, and sensing payload. A 2900 mAh battery serves as the main power source, while the PDB distributes energy to the flight controller and other UAV components.

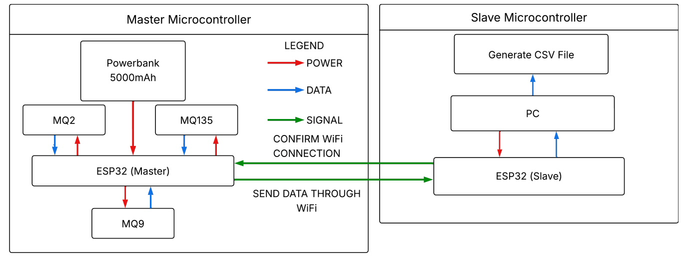

Figure 3. Gas Module Block Diagram

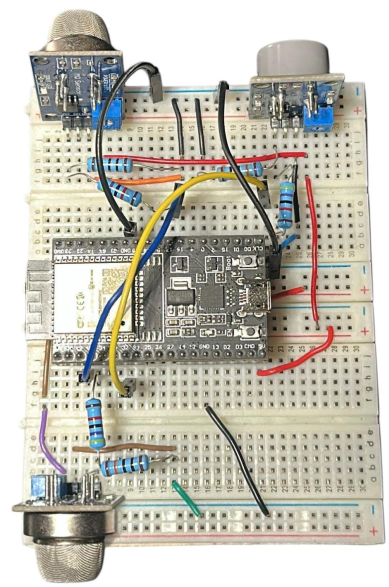

Figure 4. Gas Module Prototyped Assembly with ESP32

The telemetry antenna is connected to the flight controller to enable bidirectional communication through the TELEM1 port, allowing transmission of flight data and control commands. Similarly, the GPS module, connected via the GPS1 port, provides positioning and navigation information that is essential for the drone's autonomous functions.

The Pixhawk is also linked to the Power Management Board (PM07 PMB), which regulates the power supply and distributes control signals to the ESCs, as well as to an onboard OAK-D Pro camera used for image analysis and visualization. The ESCs convert the PWM signals from the Pixhawk into control signals, generating the thrust required for flight. The integration of these components ensures efficient interaction between power, control, and communication subsystems, providing stability and precision to the UAV during its missions.

The gas module architecture shown in Fig. 3, Fig. 4, and Fig. 5 represents the ESP32-based sensing architecture used for the test campaigns. Across Caguas, Juncos, and Gurabo, the same master-slave wireless architecture was maintained; sensor connections were modified as needed for each measurement campaign.

C. MQ Sensor Measurement Model

MQ-series sensors operate as heated metal-oxide semiconductor devices whose sensing resistance varies with gas

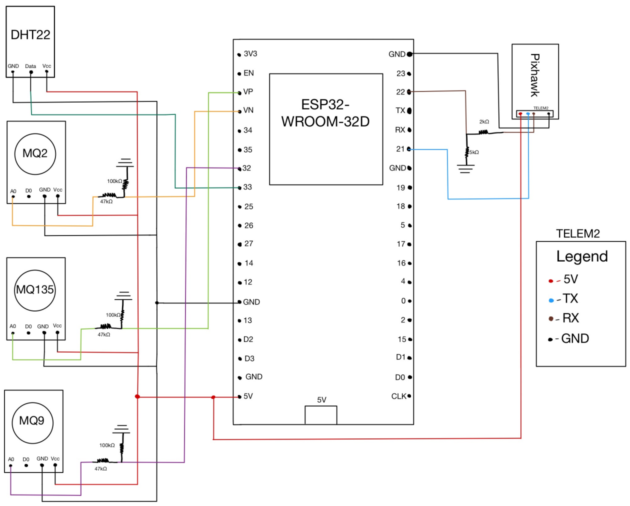

Figure 5. Gas Module Schematic with ESP32

exposure. The sensor output is measured as the voltage across the load resistor R_L, allowing the sensing resistance R_s to be calculated as

$$R_s = R_L \left(\frac{V_C}{V_{RL}} - 1 \right) \tag{1}$$

where V_C is the sensor supply voltage and V_{RL} is the measured analog output voltage. To reduce sensor-to-sensor variation, readings are normalized using a baseline resistance R_0 measured under reference environmental conditions:

$$R_r = \frac{R_s}{R_0} \tag{2}$$

Gas concentration-equivalent values are estimated from log-log sensitivity curves reported in MQ sensor documentation. For each target gas, two representative datasheet points are selected, where x is gas concentration in ppm and y is the corresponding R_s/R_0 ratio. The curve slope and intercept are

$$m = \frac{\log(y_2) - \log(y_1)}{\log(x_2) - \log(x_1)} \tag{3}$$

$$b = \log(y_1) - m \log(x_1) \tag{4}$$

Using these coefficients, the ppm-equivalent estimate is obtained from

$$\log(\text{ppm}) = \frac{\log(R_r) - b}{m} \tag{5}$$

For the Caguas-Juncos test campaign, ppm outputs are treated as raw data, voltage-derived concentration equivalent indicators while the Gurabo test campaign's ppm outputs are treated as concentration-equivalent indicators derived from MQ sensitivity curves rather than reference-grade absolute measurements. For the Gurabo tests, additional baseline calibration and parametrization were performed for the MQ-2 and MQ-9 configuration by calculating R_0 from the measured baseline environment before converting readings into ppm-equivalent values. Because MQ sensors exhibit cross-sensitivity and environmental dependence, interpretation is paired with temperature, humidity, and pressure data whenever available [14], [15], [19]–[22].

D. ESP32-Based Monitoring Logic

The ESP32 sensing node improves monitoring by combining acquisition, preprocessing, and wireless transmission in one onboard unit. Analog MQ readings are converted to voltage and used to compute R_s and R_r. When included in the sensor configuration, BME/BMP280 measurements are acquired and appended to the record. After a stabilization interval, each cycle is formatted as a CSV-compatible record and transmitted wirelessly to the receiving ESP32 or monitoring station, while selected values remain compatible with MAVLink telemetry.

III. Test Description

Testing was performed in three distinct geographic locations in Puerto Rico's central-eastern region for data comparison of atmospheric measurements in both areas. Each test had an operational duration of one hour. To ensure measured results were replicable and could be correlated to historical environmental data, GPS coordinates and altitude from sea level were included as test parameters due to their effect on atmospheric gas concentrations.

The Juncos test was performed at a latitude of 18.21727° N and longitude 65.89968° W to an altitude of 80 meters above sea level, measured through the internal GPS system connected to the UAV flight controller. Indoor testing altitude was measured at 1.5 meters from the ground and is included in the aforementioned altitude test. The test was conducted indoors at a residential kitchen equipped with basic household appliances such as a refrigerator, a gas stove, and a microwave and no known sources of pollution or noxious emissions near the sensor array.

The Caguas test was performed at a latitude of 18.23954° N, and longitude 66.00526° W to an altitude of 65 meters above sea level, using the internal GPS system from the UAV flight controller. Indoor testing altitude was measured at 2.1 meters from the ground and is included in the aforementioned altitude test. It was conducted inside a university laboratory where electrical and mechanical work is performed, with no known sources of pollution or noxious emissions near the sensor array.

Testing conditions were replicated as per the first test in Juncos by measuring inside an indoor environment to attain comparable results with approximately similar environment variables. Elevation, coordinates and indoor setting for each test were used as the main reference point for comparing the concentration changes of each gas.

Additional testing was conducted in Gurabo, Puerto Rico, using the same ESP32-based sensing architecture with a modified sensor configuration. These tests were performed at approximately 18°14'21"N, 66°00'19"W and 67 m elevation. Test 1 was performed indoors from 1:08 PM to 2:08 PM, while Test 2 was performed outdoors from 4:23 PM to 5:23 PM. The Gurabo configuration included MQ-2, MQ-9, and BME/BMP280 measurements to evaluate indoor baseline behavior and outdoor atmospheric variability.

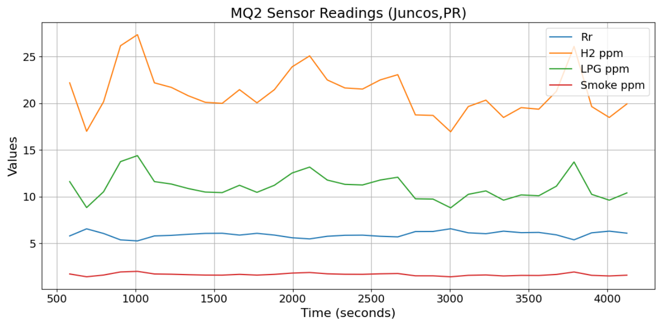

Figure 6. MQ2 Sensor Readings in Juncos, PR

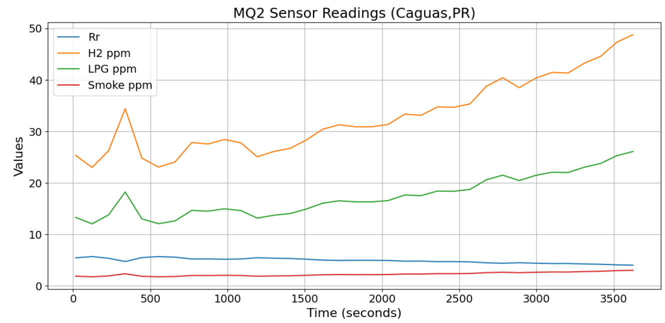

Figure 7. MQ2 Sensor Readings in Caguas, PR

IV. Results and Discussions

A. Environmental Comparison of Test Conditions

The Caguas and Juncos test campaign is presented first to establish the comparative behavior of the ESP32-based sensing platform under two indoor environments. The MQ-2 results in Fig. 6 and Fig. 7 compare combustible-gas trends in Juncos and Caguas, respectively, while the MQ-9 results in Fig. 8 and Fig. 9 compare combustion-related gas behavior for the same locations. The MQ-135 measurements in Fig. 10 and Fig. 11 provide additional air-quality reference trends for Caguas and Juncos before the Gurabo indoor and outdoor tests are discussed.

The Gurabo test campaign is presented to establish the comparative behavior of the sensing platform under two adjacent localized environments but divergent ambient conditions. The indoor test generated the environmental readings shown in Fig. 12 through Fig. 17, while the outdoor test generated the results shown in Fig. 18 through Fig. 23.

The indoor test provides a baseline with minimal airflow and stable ambient conditions that were intentionally disturbed to generate variations in the sensor readings by changing air quality and introducing impurities, while the outdoor test introduces natural temperature variation, humidity changes, and airflow disturbances without direct intervention from testing personnel.

As MQ-series MOS sensors require heater stabilization and their resistance response depends on ambient conditions, a warm-up interval and a consistent baseline definition (R_0) are recommended before interpreting R_s/R_0 trends across sessions [14], [19]–[21].

B. Mathematical Comparison of Test Conditions

The Caguas, Juncos, and Gurabo datasets were evaluated using mean value and linear trend slope. For a measured channel x_i, the mean value is

$$\bar{x} = \frac{1}{N}\sum_{i=1}^{N} x_i \tag{6}$$

and the temporal trend is represented by the linear regression slope

$$m = \frac{N\sum xy - \sum x \sum y}{N\sum x^2 - (\sum x)^2} \tag{7}$$

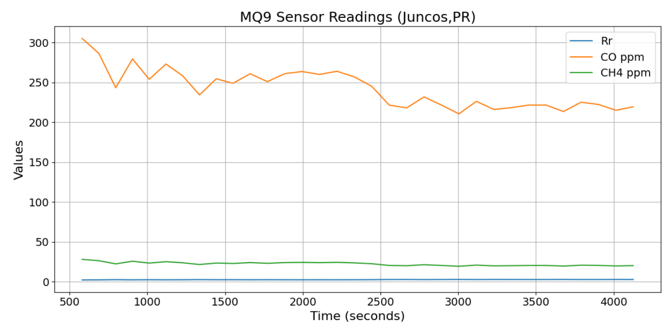

Figure 8. MQ9 Sensor Readings in Juncos, PR

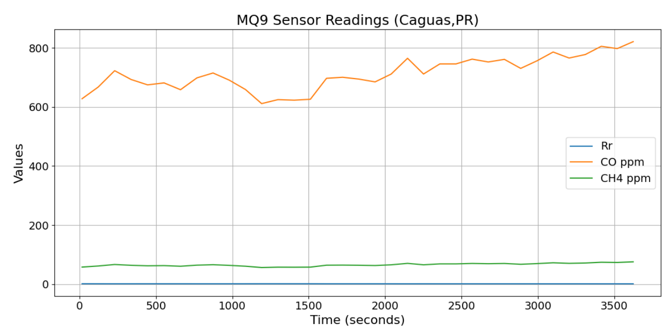

Figure 9. MQ9 Sensor Readings in Caguas, PR

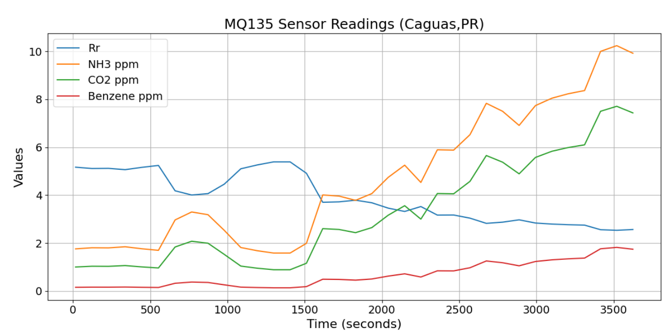

Figure 10. MQ135 Sensor Readings in Caguas, PR

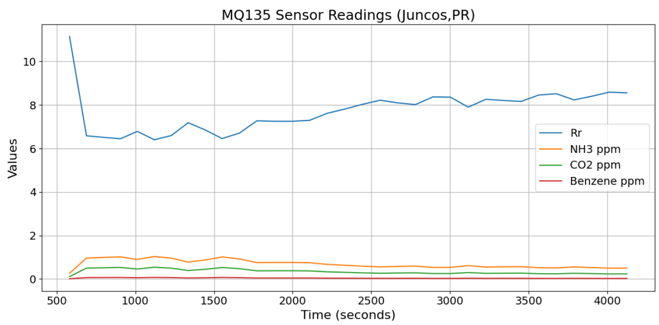

Figure 11. MQ135 Sensor Readings in Juncos, PR

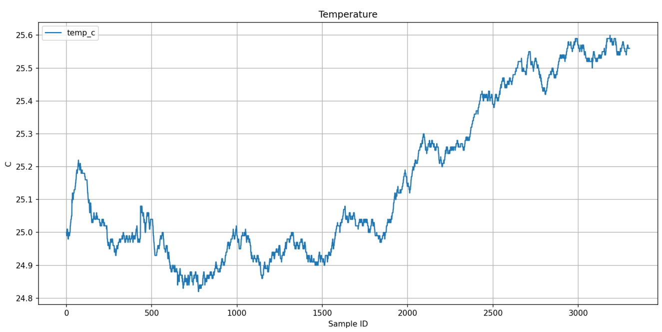

Figure 12. BME/BMP280 Indoor Temperature Test in Gurabo, PR.

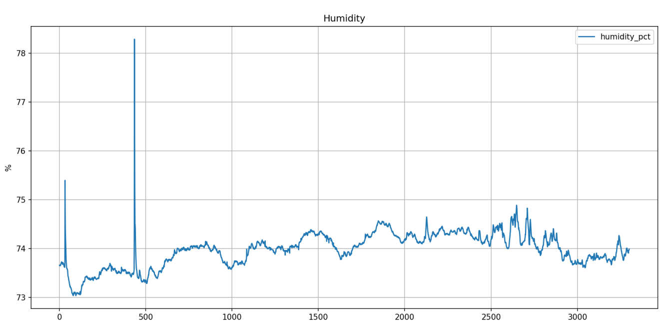

Figure 13. BME/BMP280 Indoor Humidity Test in Gurabo, PR.

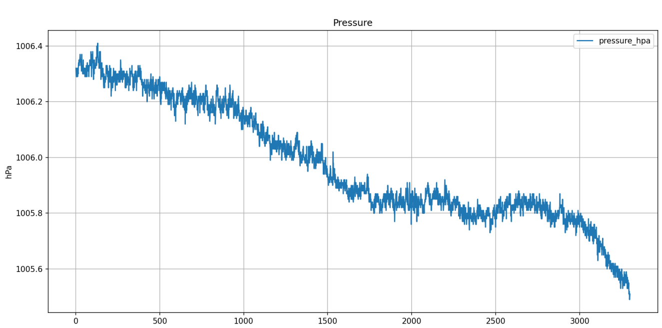

Figure 14. BME/BMP280 Indoor Pressure Test in Gurabo, PR.

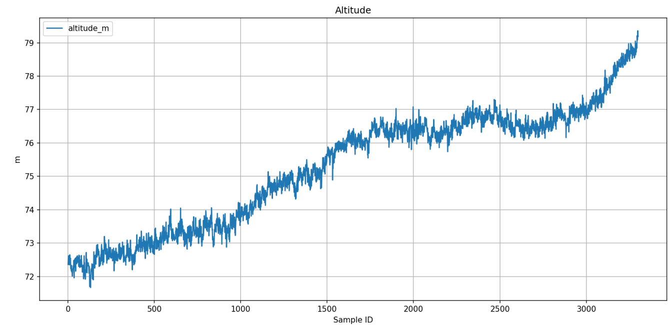

Figure 15. BME/BMP280 Indoor Pressure-derived Altitude Test in Gurabo, PR.

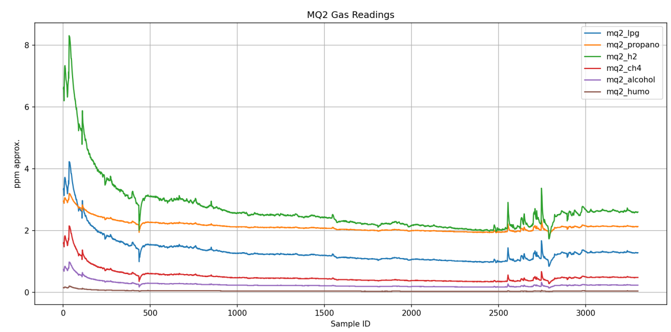

Figure 16. Indoor MQ-2 Test in Gurabo, PR.

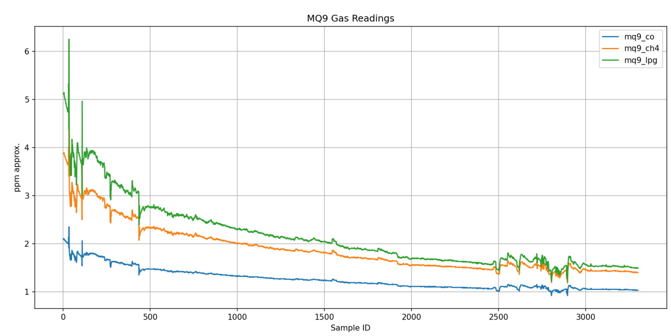

Figure 17. Indoor MQ-9 Test in Gurabo, PR.

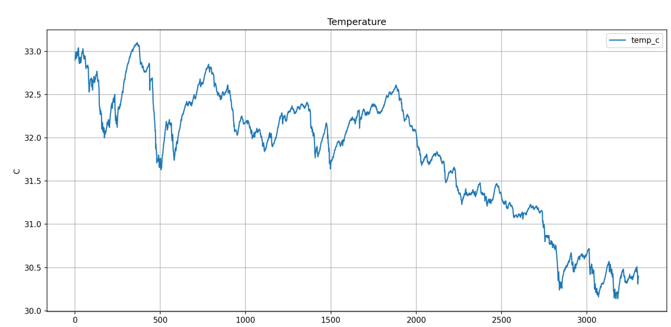

Figure 18. BME/BMP280 Outdoor Temperature Test in Gurabo, PR.

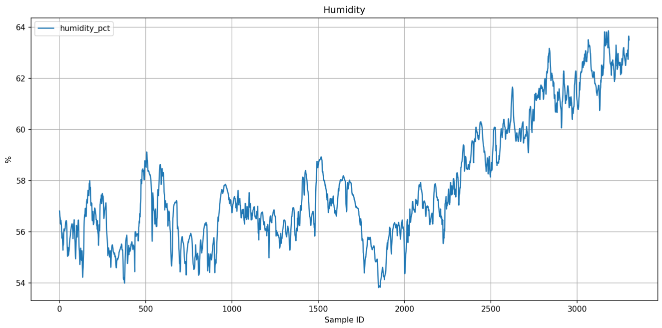

Figure 19. BME/BMP280 Outdoor Humidity Test in Gurabo, PR.

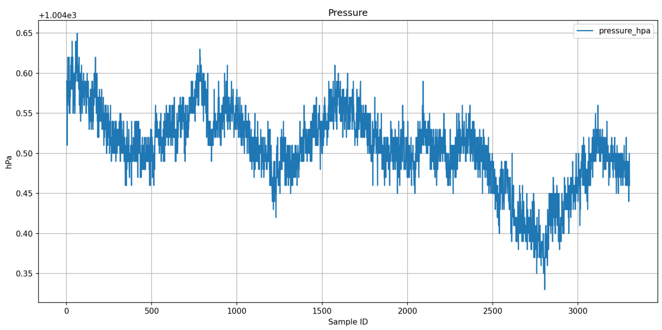

Figure 20. BME/BMP280 Outdoor Pressure Test in Gurabo, PR.

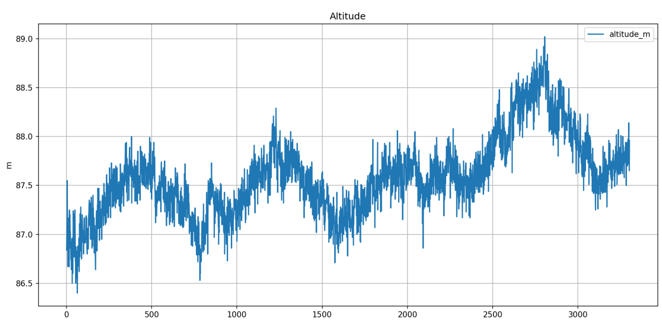

Figure 21. BME/BMP280 Outdoor Pressure-derived Altitude Test in Gurabo, PR.

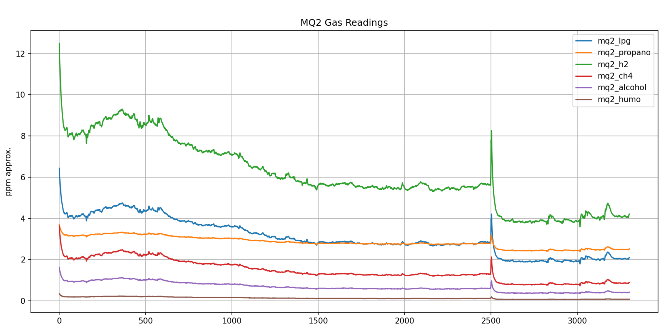

Figure 22. Outdoor MQ-2 Test in Gurabo, PR.

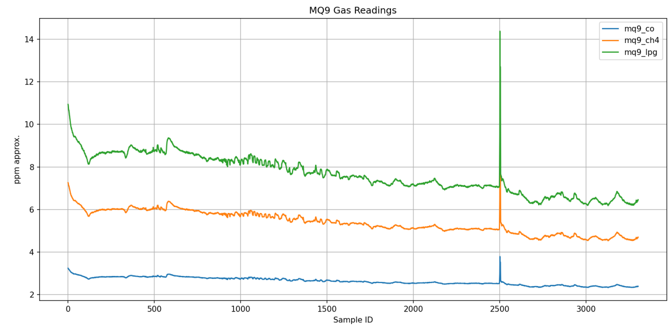

Figure 23. Outdoor MQ-9 Test in Gurabo, PR.

Table I
SUMMARY OF KEY GAS CHANNELS IN CAGUAS AND JUNCOS

Channel (ppm)	Mean Caguas	Mean Juncos	Slope Caguas	Slope Juncos
CO (MQ-9, mq9_co_ppm)	710.93	236.49	142.57	-64.17
CH_4 (MQ-9)	65.41	21.76	13.12	-5.90
CO_2 (MQ-135)	3.23	0.34	6.76	-0.29
Benzene (MQ-135)	0.67	0.04	1.63	-0.05
LPG (MQ-2)	17.24	10.45	12.42	-0.56
Smoke (MQ-2)	2.25	1.59	1.13	-0.06

where m represents the rate of change of the measured channel over time. Positive slopes indicate increasing pollutant-equivalent trends, while negative or near-zero slopes indicate decreasing or stable behavior.

The statistical summary presented in Table I reveals systematic differences in gas concentration-equivalent behavior between Caguas and Juncos. Because MQ-series sensors are MOS devices, their output is interpreted through resistance variation and the normalized ratio R_s/R_0 reported in vendor documentation [14], [15], [19]. Lower R_s/R_0 values indicate higher aggregate gas loading, but low-cost MOS sensors are affected by cross-sensitivity, temperature, and humidity [20]–[22]. Therefore, the reported ppm values are interpreted as concentration-equivalent indicators rather than reference-grade absolute measurements.

Caguas exhibited higher mean values and positive slopes in the main gas channels, while Juncos showed lower values and mostly negative or near-zero slopes. This behavior is summarized in Table I and Fig. 24, indicating stronger pollutant-equivalent accumulation in Caguas and more stable baseline behavior in Juncos.

The Gurabo comparison is based on Test 1 and Test 2 measurements shown in Fig. 12–Fig. 17 and Fig. 18–Fig. 23. Test 1 produced stable indoor behavior, with temperature near 25°C, humidity near 73–75%, gradual pressure drift, and MQ-2/MQ-9 convergence toward baseline. Test 2 showed stronger variability, including decreasing temperature, increasing humidity, pressure-derived altitude drift, and transient MQ peaks. This confirms that indoor measurements are suitable for baseline calibration, while outdoor measurements evaluate real-world behavior under airflow, humidity, and temperature variation.

C. Combustible Gas Behavior Measured by MQ-2

The MQ-2 sensor responds to combustible gases such as hydrogen, LPG, and smoke through resistance changes in its

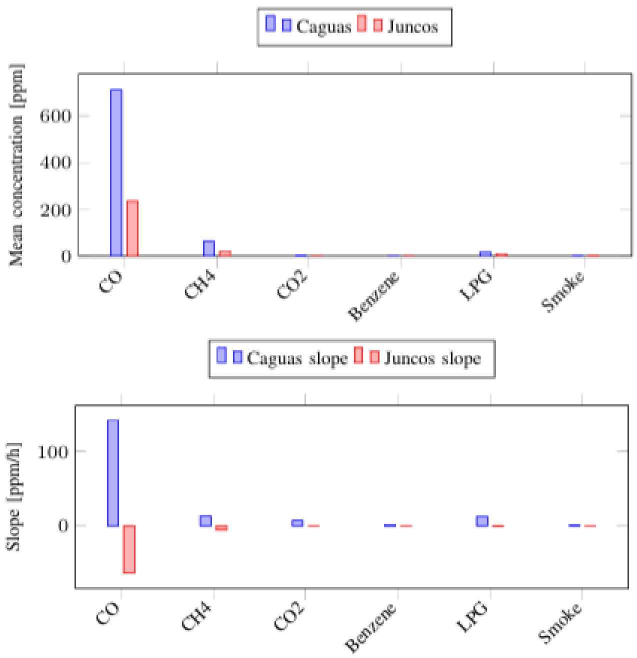

Figure 24. Mean Concentrations and Linear Trend Slopes Comparison for Caguas-Juncos Test Campaign.

MOS sensing layer. Across the ESP32-based test campaigns, MQ-2 readings provided relative combustible-gas trends under each sensor configuration. In the Caguas and Juncos tests, Caguas showed higher MQ-2 concentration-equivalent values than Juncos. As shown in Fig. 7, LPG in Caguas increased from approximately 15 ppm to nearly 40 ppm, while Fig. 6 shows that Juncos remained near 10–15 ppm with a slight negative trend.

The Gurabo MQ-2 results follow the expected MOS behavior: Test 1 stabilizes toward an indoor baseline, while Test 2 shows larger outdoor variability. This supports using MQ-2 as a relative combustible-gas trend indicator when interpreted with environmental context.

D. Combustion-Related Gases Detected with MQ-9

The MQ-9 sensor is sensitive to combustion-related gases such as carbon monoxide and methane. In Caguas, Fig. 9 shows CO increasing from approximately 600 ppm to over 800 ppm, with a positive trend of $+142.6$ ppm/h. Methane follows a similar upward trajectory [23]. In contrast, Fig. 8 shows CO in Juncos decreasing toward approximately 220 ppm, with a slope of -64.17 ppm/h.

The Gurabo MQ-9 results reinforce this interpretation: indoor readings provide a stable baseline, while outdoor readings show transient peaks caused by environmental variability and possible localized combustion-related disturbances.

E. Air Quality Trends Observed with MQ-135

The MQ-135 sensor was used in the Caguas/Juncos dataset. As shown in Fig. 10, Caguas exhibited increasing estimated CO_2, NH_3, and benzene trends, including a CO_2 slope of $+6.76$ ppm/h [24]. In contrast, Fig. 11 shows that Juncos remained close to baseline with minimal temporal variation.

For Gurabo, the MQ-135 sensor was not used; instead, the sensor configuration emphasized MQ-2, MQ-9, and BME/BMP280 measurements to compare indoor and outdoor behavior. This represents a sensor-set modification within the same ESP32-based sensing architecture, not a change in system architecture.

F. Structured Sensor Behavior and Cross-Channel Correlation

Across the Caguas/Juncos dataset, pollutant-equivalent channels derived from each MQ sensor show strong positive correlation with one another and inverse correlation with the normalized resistance ratio R_r. This behavior is consistent with the MQ operating principle, where increased gas exposure reduces sensing resistance relative to baseline. For MQ-135, the inverse correlation is stronger in Caguas ($r \approx -0.94$) than in Juncos ($r \approx -0.18$), reflecting a wider dynamic response under higher pollutant-equivalent variability.

Results show that MQ-series sensors provide useful relative trends when paired with environmental measurements. The Gurabo tests address calibration and environmental-compensation concerns by adding baseline interpretation and BME/BMP280 context while preserving the same ESP32-based wireless sensing architecture. Future work will include variance metrics, uncertainty bounds, and confidence intervals to strengthen quantitative comparison.

V. Conclusions

This work presents the design and implementation of an autonomous UAV platform for environmental monitoring that combines a Pixhawk 6C flight controller with a dual ESP32 master-slave wireless sensing architecture. The sensing node interfaces with selected MQ gas sensors and environmental sensors depending on the test configuration, while wireless transmission supports logging and MAVLink-compatible telemetry.

Field tests performed in Caguas and Juncos, Puerto Rico, showed that the system can collect geo-referenced measurements and distinguish environments with different combustion-related and urban emission trends. Caguas exhibited higher average concentrations and positive temporal trends, while Juncos presented lower reference values and generally flat or decreasing trends. Gurabo tests used the same ESP32-based architecture with a modified sensor set consisting of MQ-2, MQ-9, and BME/BMP280 measurements. Test 1 established a stable indoor baseline, while Test 2 demonstrated outdoor atmospheric variability. The results confirm that MQ-series sensors provide useful relative trends when interpreted with environmental context, but should not be treated as reference-grade instruments without calibration and compensation.

VI. Acknowledgment

We appreciate the support received by the Universidad Ana G. Méndez, Gurabo campus and Collins Aerospace. Special mention to Dr. Miguel Goenaga for his support in this project.

References

[1] R. T. Coifman *et al.*, “Drone-based delivery for medical and disaster relief: A review,” *IEEE Transactions on Automation Science and Engineering*, vol. 19, no. 3, pp. 2312–2325, 2022.

[2] M. R. Abdalla, “Recent advances in UAV technology: A review,” *IEEE Access*, vol. 10, pp. 103456–103478, 2022.

[3] P. Doherty and P. Rudol, “A UAV search and rescue scenario with human body detection and geolocalization,” in *Proc. 20th Int. Conf. on Artificial Intelligence*, (Hyderabad, India), pp. 1–8, 2007.

[4] L. Merino, F. Caballero, J. R. Martínez-de-Dios, I. Maza, and A. Ollero, “An unmanned aircraft system for automatic forest fire monitoring and measurement,” *Journal of Intelligent & Robotic Systems*, vol. 65, no. 1–4, pp. 533–548, 2012.

[5] D. Molloy, *Exploring Raspberry Pi: Interfacing to the Real World with Embedded Linux*. Wiley, 2016.

[6] F. Nex and F. Remondino, “UAV for 3D mapping applications: A review,” *Applied Geomatics*, vol. 6, no. 1, pp. 1–15, 2014.

[7] MAVLink Project, “Mavlink developer guide.” Online Documentation. Accessed: Jan. 2026.

[8] PX4 Development Team, “Mavlink messaging.” PX4 User Guide. Accessed: Jan. 2026.

[9] MAVLink Project, “Mavlink common message set (common.xml).” Online Documentation. Accessed: Jan. 2026.

[10] ArduPilot Dev Team, “Mavlink basics.” ArduPilot Developer Documentation. Accessed: Jan. 2026.

[11] PX4 Development Team, “Custom mavlink messages.” PX4 User Guide. Accessed: Jan. 2026.

[12] S. Garrido-Jurado, R. Muñoz-Salinas, F. J. Madrid-Cuevas, and M. J. Marín-Jiménez, “Automatic generation and detection of highly reliable fiducial markers under occlusion,” *Pattern Recognition*, vol. 47, no. 6, pp. 2280–2292, 2014.

[13] OpenCV Team, “Detection of ArUco markers.” OpenCV Documentation. Accessed: Jan. 2026.

[14] P. Corporation, “Mq-2 gas sensor carrier with voltage regulator.” Pololu Product Documentation, 2023. Accessed: Jan. 2026.

[15] L. Haoyue Electronics Co., “MQ-9 gas sensor datasheet.” Product Documentation. Accessed: Jan. 2026.

[16] PX4 Development Team, “Holybro pixhawk 6C.” PX4 User Guide. Accessed: Jan. 2026.

[17] ArduPilot Dev Team, “Pixhawk 6C / 6C mini flight controller.” ArduPilot Documentation. Accessed: Jan. 2026.

[18] Holybro, “Pixhawk 6C technical specification.” Product Documentation. Accessed: Jan. 2026.

[19] Hanwei Electronics Co., Ltd., “MQ-135 gas sensor technical data.” Datasheet (PDF). Accessed: Jan. 2026.

[20] I. Hayward *et al.*, “Low-cost air quality sensors: Biases, corrections and practical considerations,” *Atmosphere*, 2024. Accessed: Jan. 2026.

[21] S. Feng *et al.*, “Review on smart gas sensing technology,” *Sensors*, 2019. Accessed: Jan. 2026.

[22] A. Lewis *et al.*, “Low-cost sensors for the measurement of atmospheric composition,” tech. rep., World Meteorological Organization (WMO), 2018. Accessed: Jan. 2026.

[23] Dräger, “Introduction to gas detection systems.” Technical White Paper. Accessed: Jan. 2026.

[24] M. Verma, M. Pant, and V. Snásel, “A comprehensive review on NSGA-II for multi-objective combinatorial optimization problems,” *IEEE Access*, vol. 9, pp. 57757–57791, 2021.